

Article

Study on the Feasibility and Performance Evaluation of High-Orbit Spacecraft Orbit Determination Based on GNSS/SLR/VLBI

Zhengcheng Wu ^{1,2,†}, Shaojie Ni ^{1,2,*}, Wei Xiao ^{1,2,†}, Zongnan Li ^{1,2} and Huicui Liu ³

¹ College of Electronic Science and Technology, National University of Defense Technology, Changsha 410073, China

² Key Laboratory of Satellite Navigation Technology, Changsha 410073, China

³ Beijing Aerospace Control Center, Beijing 100094, China

* Correspondence: nishaojie@nudt.edu.cn

† These authors contributed equally to this work.

Abstract: Deep space exploration utilizing high-orbit vehicles is a vital approach for extending beyond near-Earth space, with orbit information serving as the foundation for all functional capabilities. The performance of orbit determination is primarily influenced by observation types, errors, geometrical structures, and physical perturbations. Currently, research on orbit determination for high-orbit spacecraft predominantly focuses on single observation methods, error characteristics, multi-source fusion techniques, and algorithms. However, these approaches often suffer from low observation accuracy and increased costs. This paper advocates for the comprehensive utilization of existing multi-source observation methods, such as GNSS (Global Navigation Satellite System), SLR (Satellite Laser Ranging), and VLBI (Very Long Baseline Interferometry), in research. The decoupled Kalman filter reveals a positive correlation between measurement positioning accuracy and orbit determination accuracy, and it derives a simple orbit performance evaluation model that considers the influence of observation value types and geometric configurations, without the need to introduce complex dynamic models. Simulations are then employed to verify and analyze antenna gain, observation values, and performance evaluation. The results indicate the following: (1) Under simulated conditions, the optimal strategy involves employing the SLR/VLBI dual system during periods when VLBI orbit determination is feasible, yielding an average Weighted Position Dilution of Precision (WPDOP) of 26.79. (2) For periods when VLBI orbit determination is not feasible, the optimal approach is to utilize the GNSS/SLR/VLBI triple system, resulting in an average WPDOP of 16.32. (3) The orbit determination performance of the triple system is not significantly impacted by the use of global SLR stations compared to using only Chinese SLR stations. However, the global network enables continuous, round-the-clock orbit determination capabilities.

Keywords: high-orbit vehicle; GNSS/SLR/VLBI; Kalman filter decoupling; orbit determination performance evaluation model; WPDOP



Citation: Wu, Z.; Ni, S.; Xiao, W.; Li, Z.; Liu, H. Study on the Feasibility and Performance Evaluation of High-Orbit Spacecraft Orbit Determination Based on GNSS/SLR/VLBI. *Remote Sens.* **2024**, *16*, 4214. <https://doi.org/10.3390/rs16224214>

Academic Editor: Baocheng Zhang

Received: 9 September 2024

Revised: 3 November 2024

Accepted: 8 November 2024

Published: 12 November 2024



Copyright: © 2024 by the authors. Licensee MDPI, Basel, Switzerland. This article is an open access article distributed under the terms and conditions of the Creative Commons Attribution (CC BY) license (<https://creativecommons.org/licenses/by/4.0/>).

1. Introduction

As outer space exploration intensifies and awareness of Earth's finite resources grows, humanity continues to advance deep space exploration technologies [1]. Over the past 20 years, medium- to high-orbit satellites have constituted about 35% of the total satellites launched, while deep space exploration vehicles have made up approximately 5% [2]. The push toward high-orbit and deep space exploration is in full swing. Programs like the United States' Artemis, the European Space Agency's EL3 (European Large Logistics Lander), and China's Chang'e series underscore the escalating interest in lunar exploration and the burgeoning desire for lunar resources, making high-precision orbit determination technology for high-orbit spacecraft in cislunar space increasingly critical [3–6].

Current research on orbit determination primarily emphasizes the integration of orbit dynamics with measurement positioning techniques, particularly those involving positioning using the GNSS [7,8]. Precise orbit determination is essentially about finding the optimal solution to the coupling of the dynamical state equation and the observation equation. Satellites move in approximately elliptical orbits around the Earth under the influence of Earth's gravity, adhering to Newton's laws of mechanics. However, factors such as the uneven distribution of Earth's mass, gravitational influences, atmospheric drag, and solar radiation pressure complicate the actual satellite orbit. Presently, both dynamic and simplified dynamic orbit determination methods are widely used. A unified time and coordinate system is typically selected as the reference framework, and observation data—obtained through ranging, velocity measurement, and angle measurement—are combined with the satellite's dynamic information to achieve optimal trajectory fitting [9]. Consequently, the accuracy of satellite orbit determination is directly dependent on the coupling between the mechanical model's precision and the quality of the observation data.

In the realm of high-orbit observation and positioning technology, methods are broadly categorized into near-Earth and far-land positioning technologies. Near-Earth positioning encompasses GNSS, SLR and VLBI positioning techniques. Research into high-orbit positioning technology using GNSS remains at the feasibility analysis and testing phase [10–12]. Meanwhile, basic signal reception has already been achieved at altitudes between 34,000 km and 68,000 km [13,14]. For high-orbit spacecraft, where receivers are above the flight altitude of GNSS, the challenges include high observation noise, significant distance, and difficulty in capturing and tracking weak signal intensities [15–18]. Current research focuses on using GNSS sidelobes for high-orbit positioning, encountering limitations such as a small number of visible satellites and reduced positioning accuracy [19,20], with simulated orbit determination accuracy around 140 m for spacecraft at altitudes of 36,000 km. Utilizing VLBI ground measurement and control stations for high-orbit positioning necessitates global network deployment. However, considerations of geopolitical constraints and siting topography result in limited and concentrated available VLBI stations, marked by poor geometric configurations, short observation arcs, and high maintenance costs, allowing only one-to-one observations. Although SLR offers high measurement accuracy for high-orbit positioning, its ground stations are sparse, and the short observation arcs lead to discontinuous positioning [21]. Remote location technology includes astronomical navigation, inertial navigation, inter-satellite links, and other measurement methods. Astronomical navigation, subdivided into angle measurement, velocity measurement, and distance measurement, has seen mature applications since missions such as Deep Space 1, Mars Surveyor [22], Deep Impact [23], and China's Chang'e [24] and Tianwen [25] series, all utilizing autonomous astronomical angle measurement navigation. Current technological efforts focus on fast capture and catalog compression algorithms [26]. In 1968, the Apollo 8 spacecraft, launched by the United States, pioneered the application of the theory of determining its orbital state using the intersection of three curved surfaces. It employed a sextant as an optical navigation sensor to assist in correcting the probe's orbital information, marking the first validation of the feasibility of celestial angle measurement navigation technology [27]. In 2013, Zhang Wei et al. [28] proposed the concept of astronomical spectral velocity measurement navigation, where a detector autonomously acquires target velocity information from spectral frequency shifts without ground assistance. Research continues to enhance spectral frequency shift acquisition with high resolution and stability [29]. Meanwhile, astronomical ranging navigation, though verifying autonomous navigation via pulsars in 2017 [30], suffers from low ranging accuracy and sensor-related payload increases, resulting in kilometer-scale ranging accuracy. A 2019 X-ray pulsar navigation test by the Chinese Academy of Sciences' Institute of High Energy Physics achieved a positioning accuracy of 10 km. Inertial navigation research focuses on fusing positioning technology with other information sources to mitigate its intrinsic error accumulation over time, commonly used for subsequent correction and prediction, thus not further explored in this paper. Inter-satellite link research currently targets the LiAISON (Linked Autonomous Interplanetary

Satellite Orbit Navigation) algorithm [31] and quantum navigation technology [32], both still in the developmental stages. In summary, a singular information source no longer suffices for high-orbit and high-precision orbit determination needs. There is a pressing need to explore the design of an Earth–Moon collaborative positioning and navigation timing system and to delve into navigation technologies that deeply integrate multi-source information. Combining various navigation methods such as radio measurement, stellar navigation, image navigation, and inertial navigation at the information and signal layers to create an integrated navigation system represents the trend and future innovation in high-precision orbit determination, also reflecting the rapid developmental trajectory for low orbit applications.

Current multi-source fusion navigation technology for high-orbit navigation primarily focuses on integrating GNSS with Earth–Moon constellations, as well as astronomical and inertial navigation systems. As GNSS performance diminishes with increasing distance from Earth, it fails to deliver high-precision navigation services for lunar space users. Consequently, researchers are exploring multi-sensor integration to achieve more accurate spacecraft state estimation. In 2014, Capuano et al. [33] initiated efforts to realize integrated navigation in ultra-high orbits, proposing a combination of INS (Inertial Navigation System), GNSS, star trackers, and orbital light filters to enhance accuracy and robust navigation performance. Autonomous navigation systems are being developed to provide real-time autonomous navigation and attitude determination for LEO (Low Earth Orbit), GEO (Geostationary Orbit), and even higher Earth orbit missions [34,35], reflecting the future trend in deep space exploration. However, there is limited research on integrating ground measurement and control stations, such as those for high-orbit space, VLBI, and SLR. With advancements in low-orbit satellite technology, VLBI and SLR technologies are expected to be deployed on low-orbit satellites to achieve autonomous navigation. Additionally, the Moonlight program by ESA (European Space Agency) [36] and the LuGRE (Lunar Gateway Research and Exploration) program by the United States [37] aim to achieve breakthroughs in GNSS navigation technology on the Moon. Therefore, studying the integration of GNSS, VLBI, and SLR technologies is essential.

In the in-depth study of integrated sensors and fusion algorithms in aircraft, various multi-sensor integration methods and adaptive algorithms have been proposed [38]. Current navigation filtering methods are primarily divided into batch processing and recursive methods. Batch filtering methods are relatively straightforward and do not require prior information. By leveraging historical data, they can theoretically yield more accurate results. These characteristics give batch filtering methods a significant advantage in general ground-based orbit determination computations, and have been successfully applied to missions such as Deep Space-1 and Deep Impact [39]. Recursive filtering methods, on the other hand, require fewer computational resources and offer faster processing speeds, providing excellent real-time performance [40,41]. For Gaussian noise and non-linear navigation systems, the EKF (Extended Kalman Filter) is effective, but it introduces truncation errors due to Taylor series expansion, which can impair performance. The UKF (Unscented Kalman Filter) method avoids these truncation errors by employing unscented transformations, improving navigation accuracy [42]. For non-Gaussian noise and non-linear systems, particle filtering offers superior filtering performance, though it suffers from particle degradation. The key to mitigating particle degradation is choosing an appropriate density function or resampling method [43]. High-orbit detection noise often exhibits low correlation and can be modeled as Gaussian noise, with the observation equations being linear. Decentralized data fusion methods, such as federated filtering, and centralized Extended Kalman Filtering are commonly used [44]. Currently, these methods are widely combined with INS and GNSS to provide autonomous navigation services for terrestrial and near-Earth vehicles, as well as lunar and Mars probes [45–47]. While batch processing methods offer significant advantages for ground-based orbit determination, the demand for higher precision in high-Earth orbits, lunar transfer trajectories, and circumlunar phases necessitates the consideration of dynamic models and spacecraft maneuvers. Furthermore,

with the deployment of low-orbit satellites and related detection methods, the requirement for real-time processing has become increasingly crucial. This trend is expected to continue in the future. Consequently, this paper opts for the Kalman filter algorithm, a recursive filtering method, to address these evolving needs. Based on the Kalman filter algorithm, this paper analyzes the relationship between orbital accuracy and geometric configuration, using it as an index to evaluate orbital accuracy.

Research on multi-source fusion techniques for ground-based navigation sources such as GNSS, SLR, and VLBI is limited but represents a future development trend. With increasing demands for real-time performance, recursive filtering methods are also emerging as a key direction for future development. In this context, this paper employs the Kalman filter algorithm to decouple the relationship between the geometric configuration and orbit determination performance of high-orbit spacecraft, aiming to highlight their potential for improving orbit determination accuracy. The study designs seven experimental combinations involving GNSS, SLR, and VLBI as single, dual, and triple systems. Considering the number of visible satellites and WPDOP values, overcoming the scarcity of data related to high-altitude spacecraft, it analyzes the orbit determination performance of high-orbit spacecraft using GNSS, SLR, and VLBI multi-source fusion from three aspects: determinable orbit periods, mean WPDOP values within the trackable period of a single VLBI station, and mean WPDOP values within the non-trackable period of a single VLBI station. Taking into account the power consumption and practical usage of VLBI and SLR, the study selects station sites in China, which is sufficient to provide research patterns for the future deployment of VLBI and SLR technologies on low-orbit satellites. At the end of the paper, global SLR sites are selected for further scientific research. However, due to the high power requirements of VLBI and the impracticality of the real-time observation of a single target using global VLBI resources, only Chinese VLBI sites are selected. Through Kalman filter decoupling, a positive correlation between the measurement positioning performance and orbit determination performance is established. The study suggests using the SLR/VLBI dual system for orbit determination during periods when a single VLBI system can determine the orbit, and adopting a GNSS/SLR/VLBI triple-system fusion strategy for other periods. The research concludes that improvements in the measurement accuracy and distribution of ground-deployed SLR and VLBI have limited impact on the performance of GNSS/SLR/VLBI triple-system orbit determination. This underscores the importance of deploying SLR and VLBI technologies on future low-orbit satellites.

2. Analytical Methods

2.1. Probabilistic Principle of Kalman Filter Algorithm

The existing orbit determination technology uses Kalman filter to fuse the dynamic model and positioning technology. This paper specifically studies the orbit determination technology based on the Kalman filter. For the navigation system, the dynamic model and positioning technology can be equivalent to a linear model.

Consider the linear system of a high-orbit vehicle described in state space:

$$\begin{cases} \mathbf{x}_k = \Phi_{k,k-1}\mathbf{x}_{k-1} + \Gamma_{k-1}\Omega_{k-1} \\ \mathbf{y}_k = \mathbf{H}_k\mathbf{x}_k + \mathbf{v}_k \end{cases} \quad (1)$$

Formula (1) contains the equation of state and the equation of observation, where k is discrete time. The corresponding state of the system at time k is $\mathbf{x}_k \in \mathbb{R}^n$. $\Phi_{k,k-1}$ is the state transition matrix, $\Omega_{k-1} \in \mathbb{R}^r$ is the state error, $\mathbf{y}_k \in \mathbb{R}^m$ is the observed signal corresponding to the state, \mathbf{H}_k is the observation matrix, and $\mathbf{v}_k \in \mathbb{R}^m$ is the observation noise. Ω_{k-1} and \mathbf{v}_k are uncorrelated Gaussian white noise with a mean of 0 and a covariance matrix of \mathbf{Q}_{k-1} and \mathbf{R}_k , respectively.

Suppose the estimate of the state quantity at the previous time, $\hat{\mathbf{x}}_{k-1}$, has a variance of P_{k-1} . It can be predicted that the state quantity $\hat{\mathbf{x}}_{k,k-1}$ at time k is

$$\hat{\mathbf{x}}_{k,k-1} = \Phi_{k,k-1}\hat{\mathbf{x}}_{k-1} \quad (2)$$

According to the covariance propagation law, the variance of the predicted value is

$$\mathbf{P}_{k|k-1} = \Phi_{k|k-1} \mathbf{P}_{k-1} \Phi_{k|k-1}^T + \mathbf{Q}_{k-1} \quad (3)$$

Finally, according to the gain matrix, the weighted sum of prediction and measurement data is obtained to obtain the state estimation $\hat{\mathbf{x}}_k$ and variance estimation \mathbf{P}_k at the next moment:

$$\hat{\mathbf{x}}_k = \hat{\mathbf{x}}_{k|k-1} + \mathbf{P}_{k|k-1} \mathbf{H}_k^T (\mathbf{H}_k \mathbf{P}_{k|k-1} \mathbf{H}_k^T + \mathbf{R}_k)^{-1} (\hat{\mathbf{y}}_k - \mathbf{H}_k \hat{\mathbf{x}}_{k|k-1}) \quad (4)$$

$$\mathbf{P}_k = \mathbf{P}_{k|k-1} - \mathbf{P}_{k|k-1} \mathbf{H}_k^T (\mathbf{H}_k \mathbf{P}_{k|k-1} \mathbf{H}_k^T + \mathbf{R}_k)^{-1} (\mathbf{H}_k \mathbf{P}_{k|k-1}) \quad (5)$$

The estimated result in the form of the final matrix is rewritten into the form of probability density, assuming that the estimated distribution after Kalman filtering is Gaussian distribution:

$$\mu_F = \mu_{Pre} + \left(\frac{H\sigma_{Pre}^2}{H^2\sigma_{Pre}^2 + \sigma_{Obs}^2} \right) (\mu_{Obs} - H\mu_{Pre}) = \frac{\mu_{Pre}\sigma_{Obs}^2 + \mu_{Obs}\sigma_{Pre}^2}{\sigma_{Pre}^2 + \sigma_{Obs}^2} \quad (6)$$

$$\sigma_F^2 = \sigma_{Pre}^2 - \left(\frac{H\sigma_{Pre}^2}{H^2\sigma_{Pre}^2 + \sigma_{Obs}^2} \right) H\sigma_{Pre}^2 = \frac{\sigma_{Pre}^2\sigma_{Obs}^2}{\sigma_{Pre}^2 + \sigma_{Obs}^2} \quad (7)$$

$$f_F(x; \mu_F, \sigma_F) = \frac{1}{\sqrt{2\pi\sigma_F^2}} \exp\left(-\frac{(x - \mu_F)^2}{2\sigma_F^2}\right) \quad (8)$$

where μ_F is the estimated mean value, σ_F^2 is the estimated variance, μ_{Pre} is the predicted mean value, σ_{Pre}^2 is the predicted variance, μ_{Obs} is the mean value of observed data, σ_{Obs}^2 is the observed variance, and $f_F(x; \mu_F, \sigma_F)$ is the probability density distribution function after estimation.

Substitute Formulas (6) and (7) into Formula (8) to further derive

$$\begin{aligned} f_F(x; \mu_{Pre}, \sigma_{Pre}, \mu_{Obs}, \sigma_{Obs}) &= \frac{1}{\sqrt{2\pi\sigma_{Pre}^2\sigma_{Obs}^2}} \exp\left(-\frac{(x - \mu_{Pre})^2 + (x - \mu_{Obs})^2}{2\sigma_{Obs}^2}\right) \\ &= f_{Pre}(x; \mu_{Pre}, \sigma_{Pre}) \cdot f_{Obs}(x; \mu_{Obs}, \sigma_{Obs}) \end{aligned} \quad (9)$$

$$f_{Pre}(x; \mu_{Pre}, \sigma_{Pre}) = \frac{1}{\sqrt{2\pi\sigma_{Pre}^2}} \exp\left(-\frac{(x - \mu_{Pre})^2}{2\sigma_{Pre}^2}\right) \quad (10)$$

$$f_{Obs}(x; \mu_{Obs}, \sigma_{Obs}) = \frac{1}{\sqrt{2\pi\sigma_{Obs}^2}} \exp\left(-\frac{(x - \mu_{Obs})^2}{2\sigma_{Obs}^2}\right) \quad (11)$$

where f_{Pre} is the predicted probability density distribution, f_{Obs} is the observed probability density distribution, and f_F is the intersection of f_{Pre} and f_{Obs} . If the variance of the observed data becomes smaller, the variance of the whole f will become smaller, that is, the positioning accuracy of the observation is positively correlated with the orbit determination accuracy. See Figure 1 for the probability distribution diagram.

In Figure 1, the high-orbit vehicle with an initial position (Time = $k - 1$) conforms to a Gaussian distribution, where the blue dashed line represents the position distribution before the prediction error. The position of the next moment can be predicted through the dynamic model, and the predicted distribution (blue solid line) presents a Gaussian distribution. The related probability density function is shown in Formula (10), which usually increases the variance. When Time = k , the measurement information is obtained by further observation, and the measurement noise also presents a Gaussian distribution (solid red line), and its probability distribution function is shown in Formula (11). At this

moment, we have two results of prediction and measurement, and the vehicle position estimate (green distribution) obtained by multiplying the two is shown in Formula (9).

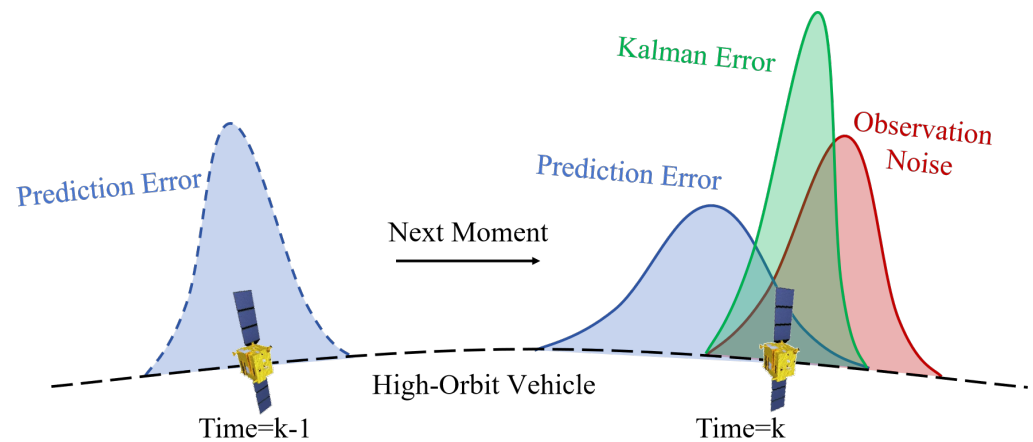


Figure 1. In the Kalman filter probability distribution diagram, the blue dotted line area is the estimated probability density distribution at the previous time, the blue solid line area is the predicted probability density distribution at the later time, the red solid line area is the observed probability density distribution at the later time, and the green solid line area is the recursive Kalman filter probability density distribution at the later time.

The above analysis shows that for the orbit determination method using Kalman filter to integrate dynamic model and positioning technology, the positioning accuracy can be used to represent the orbit determination accuracy to a certain extent.

2.2. Negative Correlation Analysis of WPDOP

GNSS, SLR, and VLBI are all ranging and positioning techniques. The observational principle of SLR is fundamentally straightforward, utilizing the time delay between the transmission and reception of laser pulses. The resulting observation equation incorporates various error terms.

For satellite observations using VLBI, the technique of differential VLBI is typically employed. In this method, when observing a target satellite, an extragalactic radio source with a precisely known position near the satellite is selected as a reference source. These sources are observed quasi-simultaneously. The amplitudes and phases of the interference fringes from both sources are then used to generate observables, which are subsequently differenced to eliminate common error influences.

Ultimately, both SLR and differential VLBI yield delay equations that are analogous to the pseudo-range observation equations in GNSS. These equations encapsulate the geometric relationships between the observing stations and the target, while accounting for various systematic and random errors inherent in each technique. And the observation equation can be uniformly simplified as Formula (12):

$$x^{(n)} = r^{(n)} + \delta t_u - \delta t^{(n)} + S^{(n)} + \epsilon_x^{(n)} \quad (12)$$

where $x^{(n)}$ is the measured distance, $r^{(n)}$ is the actual distance, δt_u is the receiving delay, $\delta t^{(n)}$ is the transmitting delay, $S^{(n)}$ is the system deviation, and $\epsilon_x^{(n)}$ is the observed random noise.

According to Formula (9), the accuracy of the observation and positioning is positively correlated with the accuracy of the orbit determination. The least square method is generally used for positioning, where the error covariance matrix is

$$\begin{aligned}
Cov \begin{pmatrix} \varepsilon_x \\ \varepsilon_y \\ \varepsilon_z \\ \varepsilon_{\delta t_1} \\ \vdots \\ \varepsilon_{\delta t_n} \end{pmatrix} &= E \left(\begin{bmatrix} \varepsilon_x \\ \varepsilon_y \\ \varepsilon_z \\ \varepsilon_{\delta t_1} \\ \vdots \\ \varepsilon_{\delta t_n} \end{bmatrix} \begin{bmatrix} \varepsilon_x & \varepsilon_y & \varepsilon_z & \varepsilon_{\delta t_1} & \cdots & \varepsilon_{\delta t_n} \end{bmatrix} \right) \\
&= E \left(\left(\mathbf{H}^T \mathbf{H} \right)^{-1} \mathbf{H}^T \varepsilon_\rho \left(\left(\mathbf{H}^T \mathbf{H} \right)^{-1} \mathbf{H}^T \varepsilon_\rho \right)^T \right) \\
&= \left(\mathbf{H}^T \mathbf{H} \right)^{-1} \mathbf{H}^T \mathbf{R} \mathbf{H} \left(\mathbf{H}^T \mathbf{H} \right)^{-1} \\
&= \left(\mathbf{H}^T \mathbf{H} \right)^{-1} \mathbf{W}
\end{aligned} \tag{13}$$

According to the ranging observation equation and Formula (13), the first three columns of \mathbf{H}_k are respectively the unit vectors of the position of the high-orbit vehicle on the rectangular coordinate axis about x , y , and z . \mathbf{R}_k represents the covariance matrix of dimension $n + 3$ with respect to ε_ρ (noise). \mathbf{W}_k is an $n + 3$ -dimensional matrix related to ε_ρ and geometric distribution, and is the amplification factor of DOP values. The reason why \mathbf{W}_k matrix is introduced is that it includes the ε_ρ and geometric distributions of different systems. When all ε_ρ are independent of each other, \mathbf{W}_k and \mathbf{R}_k are exactly the same. For Formula (11), $(\mathbf{H}_k^T \mathbf{H}_k)^{-1}$ is a diagonal matrix, and multiplying with \mathbf{W}_k is equivalent to taking its diagonal elements. The positioning accuracy x , y , and z correspond to the first three diagonal elements of the $\mathbf{W}_k(\mathbf{H}_k^T \mathbf{H}_k)^{-1}$ matrix, respectively. Still, it is only necessary to pay attention to the first three rows of diagonal elements of the $\mathbf{W}_k(\mathbf{H}_k^T \mathbf{H}_k)^{-1}$ matrix, which correspond to the positioning error computed by the GPS pseudo-distance least squares. In this paper, the square root of the sum of squares of the first three diagonal lines of the $\mathbf{W}_k(\mathbf{H}_k^T \mathbf{H}_k)^{-1}$ matrix is defined as the Weighted Position Dilution of Precision (WPDOP).

$$D_k = \mathbf{W}_k(\mathbf{H}_k^T \mathbf{H}_k)^{-1} \tag{14}$$

$$WPDOP = \sqrt{D_{k(1,1)}^2 + D_{k(2,2)}^2 + D_{k(3,3)}^2} \tag{15}$$

Obviously, when the WPDOP value is smaller, the D_k value in the corresponding Formula (15) is also smaller, and the final orbit determination accuracy of the high-orbit spacecraft is higher. It can be concluded that the WPDOP value can roughly evaluate the quality of the orbit determination accuracy, and the two are negatively correlated, providing a more convenient support method for the study of multi-system orbit determination performance of high-orbit spacecraft.

3. Simulation Strategy

3.1. Data Selection

3.1.1. High-Orbit Vehicle Distribution

The six elements of the initial orbit of the high-orbit vehicle are shown in Table 1. The starting time is set at 20:00 on 1 January 2024. The GSTAR software of Beijing University of Aeronautics and Astronautics is used for simulation and recursion of the orbital data of the high-orbit vehicle from 20:00 on 1 January 2024 to 20:00 on 6 January 2024. The simulation track diagram is shown in Figure 2.

Table 1. Table of initial position parameters of six elements of high-orbit vehicle.

\mathbf{a}	\mathbf{e}	\mathbf{i}	$\boldsymbol{\omega}$	$\boldsymbol{\Omega}$	$\boldsymbol{\phi}$
100,000 km	0	70°	0	0	0

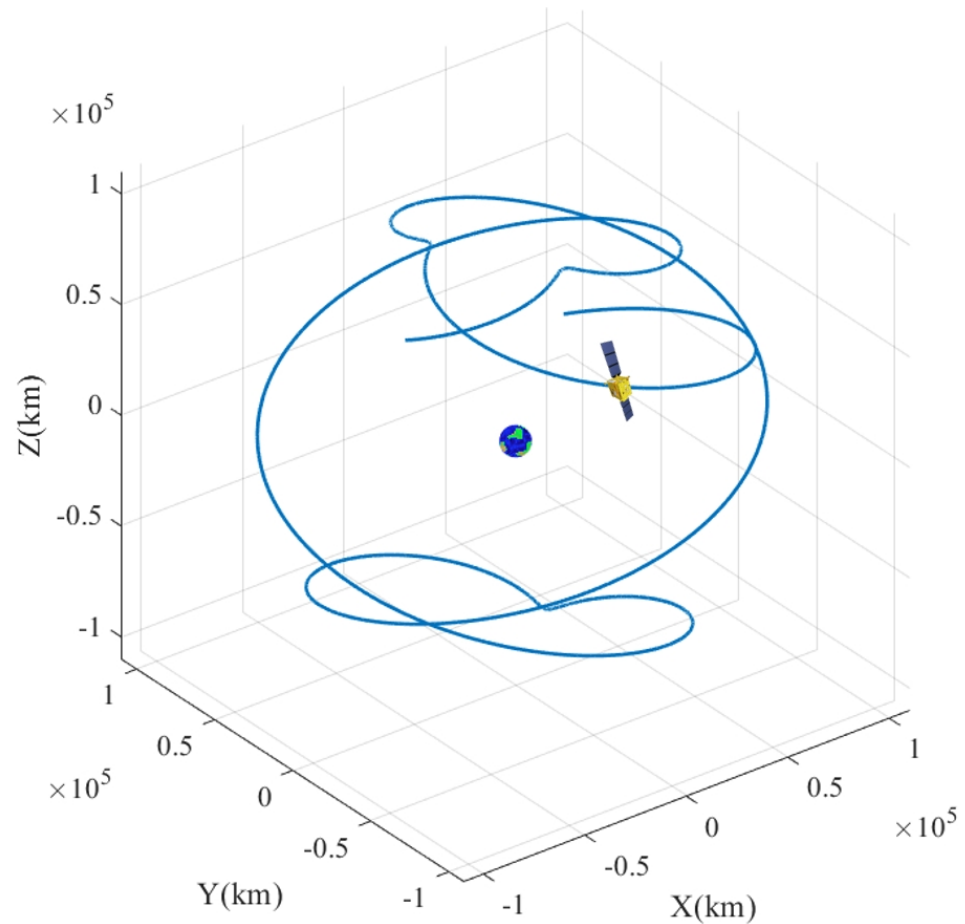


Figure 2. Position and track map of the high-orbit vehicle during the period from 20:00:00 on 1 January 2024 to 20:00:00 on 6 January 2024.

3.1.2. GNSS/SLR/VLBI Distribution and Measurement Precision

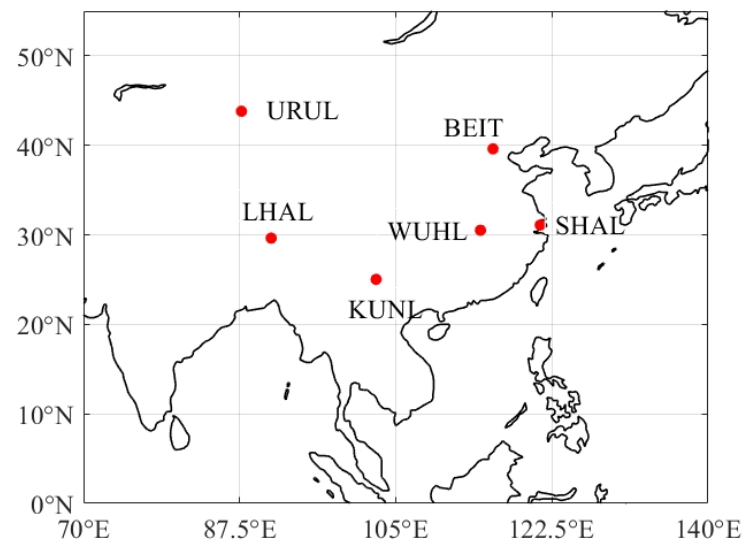
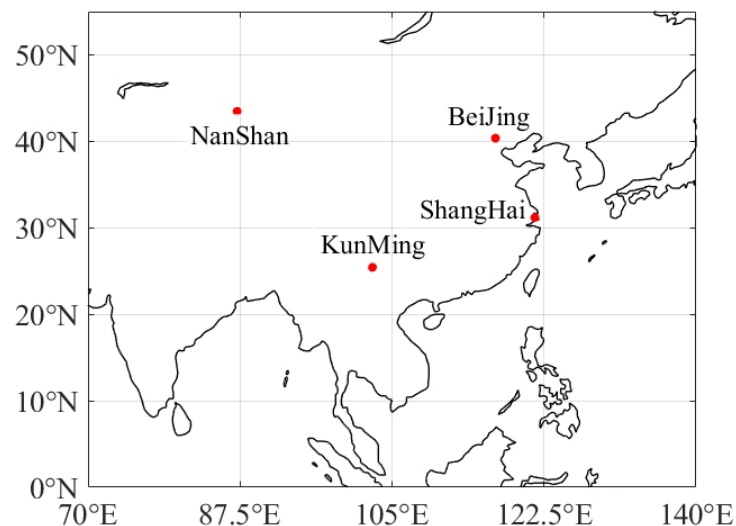
The simulation environment time range is from 20:00 on 1 January 2024 to 20:00 on 6 January 2024, with a time interval of 30 s. The GNSS measurement error is set at 20 m, and the VLBI measurement error is set at 0.5 m. The SLR system has a detection capability of 40,000 km, and the single measurement accuracy is less than 1.5 cm. The accuracy of 93% of the LLR data obtained by Tianqin laser ranging station is better than 10 cm. Therefore, for the purposes of this study, the measurement precision of SLR is provisionally and subjectively set at 0.05 m. The BDS, GPS, GLO (Globalnaya Navigatsionnaya Sputnikovaya Sistema), and GAL (Galileo) precision ephemeris data are from the IGS website download data, including 31 GPS satellites, 42 BDS satellites, 20 GLO satellites, and 24 GAL satellites; the specific breakdown of the types are shown in Table 2.

The data of global SLR stations come from the ILRS official website. This study primarily utilizes SLR stations located in China, and the distribution is shown in Figure 3. VLBI techniques are utilized in China, as in other space agencies, primarily for high-precision tracking and orbit determination of high-orbit and deep space spacecraft. The observation stations are all from domestic stations, namely, Beijing, Shanghai, Nanshan, and Kunming stations, and the coordinate positions are [31.1833°N, 121.4444°E], [25.432°N, 102.746°E], [43.4667°N, 87.1667°E], and [40.3588°N, 116.9058°E], as shown in Figure 4.

It can be seen that SLR and VLBI of four stations almost coincide, and all of them are distributed in China, with fewer stations and poor geometric distribution. It can be predicted that the WPDOP value of a single system will not be small.

Table 2. A list of the types and corresponding serial numbers of constellations.

Constellation	Type	PRN
GPS	IIF	G3 G6 G8 G9 G10 G24 G25 G26 G27 G30 G32
	IIR	G2 G13 G16 G19 G20 G21 G22
	IIR-M	G1 G5 G7 G12 G15 G17 G29 G31
	III	G4 G11 G14 G18 G23 G28
BDS	GEO/IGSO	C1 C2 C3 C4 C5 C6 C7 C8 C9 C10 C13 C16 C38 C39 C40
	MEO	C11 C12 C14 C19 C20 C21 C22 C23 C24 C25 C26 C27 C28 C29
		C30 C32 C33 C34 C35 C36 C37 C41 C42 C43 C44 C45 C46
GLO	GLO	R1 R2 R3 R4 R5 R7 R8 R9 R11 R12 R13 R14 R15 R17 R18 R19 R20 R21 R22 R24
GAL	GAL	E1 E2 E3 E4 E5 E7 E8 E9 E11 E12 E13 E14 E15 E18 E19 E21 E24 E25 E26 E27 E30 E31 E33 E36

**Figure 3.** Distribution map of SLR stations in China.**Figure 4.** Distribution map of VLBI stations in China.

3.2. Link Simulation Condition

GNSS, SLR, and VLBI are used to observe high-orbit spacecraft with a orbital altitude of 100,000 km. Both SLR and VLBI are considered to meet the link visibility conditions at

all times. While SLR and VLBI systems are currently limited to one-to-one target observations, contemporary technological advancements have successfully met the signal strength requirements for establishing robust connections. This research lays the groundwork for the potential future deployment of these technologies on Low Earth Orbit (LEO) satellites. The proliferation of LEO satellite constellations presents unique opportunities beyond the self-diagnostic capabilities of VLBI and SLR. These dense networks could facilitate target-specific navigation and positioning through strategic satellite selection. For this study, we assume successful link connections when visibility conditions are met, enabling the exploration of theoretical maximum performance in a LEO environment. With the advancement of technology, we assume that SLR can quickly switch to observing other satellites, meaning that we posit that SLR can be utilized for the detection services of high-orbit spacecraft. However, GNSS mainly serves ground users at the beginning of design, and the detection of high-orbit spacecraft can only be conducted through the leaked main lobe signal and sidelobe signal shielded by the Earth, and the signal strength is weak. Further simulation is needed to analyze whether the link meets the conditions of traceable capture solution, and then further analyze the number of visible satellites.

Considering whether the Earth blocks the GNSS signal on the opposite side of the Earth, it is necessary to establish an Earth model, and then consider the signal strength of the transmitter, antenna gain, free space loss, receiver sensitivity, receiver loss, and experience loss, and provide the following simulation data. The simulation flow chart is shown in Figure 5.

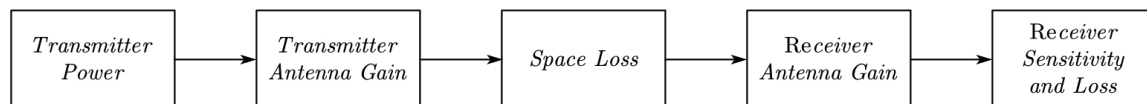


Figure 5. Radio signal link analysis flow chart.

3.2.1. Earth Elevation Model

Considering the Earth's blocking of the signal, topographic considerations of the Earth's surface are necessary. Data are obtained from the National Geographic Data Center, Oceanic and Atmospheric Administration (NOAA), U.S. Department of Commerce, Data Circular No. 88-MGG-02.

The data coordinates are transformed into the Earth-centered fixed coordinate system, the grid data of $1^\circ \times 1^\circ$ are interpolated to $0.1^\circ \times 0.1^\circ$, and the grid data are stored in a table for simulation. The data are shown in Figure 6.

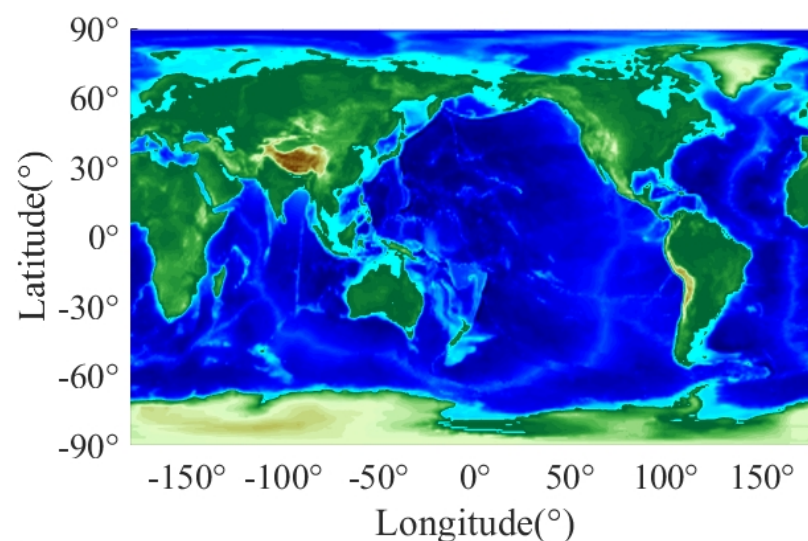


Figure 6. An elevation map of the Earth.

SLR and VLBI are located on the ground, and the minimum accepted elevation angle is set at 10° as the visual limitation. The GNSS antenna always points towards the geocentric direction. For the detection of high-orbit spacecraft, satellites on the same side of the Earth and high-orbit spacecraft cannot be used, and the detection must be carried out by the main lobe leakage signal or sidelobe signal of the opposite GNSS satellite. Therefore, link analysis is more necessary. The geometric diagram is shown in Figure 7.

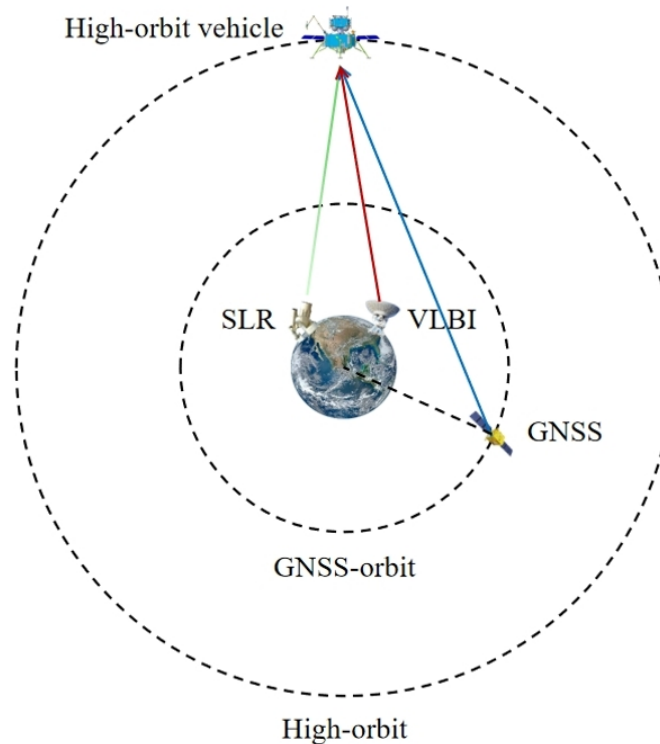


Figure 7. Geometric diagram of GNSS, SLR, and VLBI stations for high-orbit vehicle detection.

3.2.2. Transmitter Power

Table 3 lists the frequency points and transmit power corresponding to GPS, BDS, GLO and GAL constellation in the simulation. The transmit power of MEO and GEO/IGSO satellites in BDS constellation is slightly different, and the power is tentatively the same.

Table 3. Different frequency and transmitter power parameters of GPS, BDS, GLO, and GAL.

Constellation	Frequency Point/MHz	Transmitted Power/dBW
GPS	L1/1575.42	14.4
	L2/1227.60	9.7
BDS	B1/1560.098	9.0
	B2/1191.795	8.0
GLO	G1/1602.00	14.1
	G2/1246.00	12.6
GAL	E1/1575.42	10.6
	E5a/1176.45	10.6

3.2.3. Antenna Gain

Figure 8 shows L1 of Block IIR, Block IIR-M, Block IIF, and Block III GPS navigation constellations released by NASA based on the ACE (Antenna Characterization Experiment) Navigation signal transmitting antenna gain mode over the frequency channel.

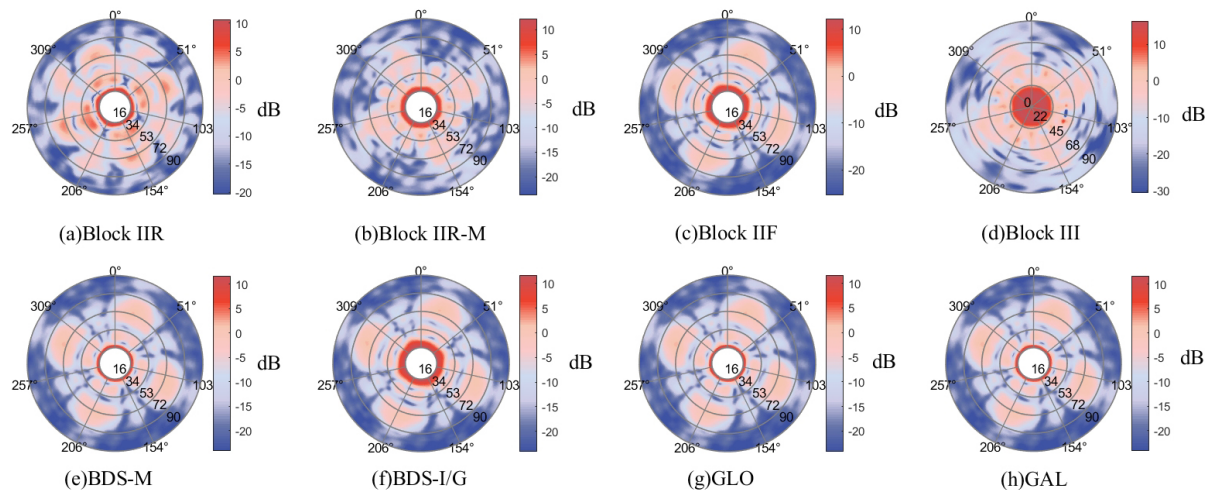


Figure 8. Directions of different types of antennas. (a) Block IIR. (b) Block IIR-M. (c) Block IIF. (d) Block III. (e) BDS-M. (f) BDS-I/G. (g) GLO. (h) GAL.

In the simulation, the signal transmission gain patterns for the other three major navigation systems are derived based on the GPS Block-IIF satellite gain pattern. Specifically, the GPS Block-IIF gain pattern is scaled by a factor of 0.95 and then projected with a scaling transformation centered on the half-power beamwidth of the main lobe. This approach is used to generate the gain patterns for each of the navigation systems under consideration.

In Figure 8, the red gain area is the main lobe area, and the gain size is reduced from 15 dB to about -5 dB. The data come from NASA's ACE (Antenna Characterization Experiment) GPS-based experiment and satellite manufacturer Lockheed Martin, which compiled the information based on its design specifications and ground test measurements of the antenna panels. For missing data with a zenith angle of less than 16° , the data source itself is missing. This paper believes that this may be due to the fact that the measurement nadir angle of the GPS antenna is set to 16° to optimize signal coverage, reduce signal occlusion interference, and ensure the effectiveness and accuracy of GPS system. With the change in the azimuth angle, the sidelobe signals are distributed in a roughly cross-shaped discrete manner, concentrated in four regions, namely, the pink region in the figure, with a gain range of -3 dB to 3 dB [48]. In order to facilitate simulation and consider the principle of having less impact on experimental results, the antenna gain is averaged on the azimuth angle, and the rough corresponding relationship between the antenna elevation and gain is obtained in Figure 9.

To address the missing gain information in the 0° – 16° range, we employ a quadratic fitting approach utilizing the main lobe data from 16° – 23° . This method is constrained to maintain continuity at 16° and to ensure that the parabola's vertex coincides with the zenith ($x = 0^\circ$). Given the sparse data distribution in the 16° – 90° range, we apply a cubic spline interpolation algorithm to generate a smooth gain profile. For the 90° – 180° range, we impose an artificial minimum gain threshold of -100 dB, acknowledging that link visibility conditions may not always be met in this range.

It is crucial to note that for the 0° – 16° range, our primary concern is to ensure that the gain exceeds 10 dB, which is the threshold for establishing link connectivity. Our fitting approach deliberately results in gain values consistently above 10 dB in this range. This decision is justified by the fact that any gain value above 10 dB is sufficient for link establishment, and further increases in gain do not affect the connectivity status. Therefore, while our approach may overestimate the actual gain values in this range, it does not impact the validity of our link visibility analysis. This method allows us to accurately assess link availability without introducing any bias or overestimation in our connectivity calculations.

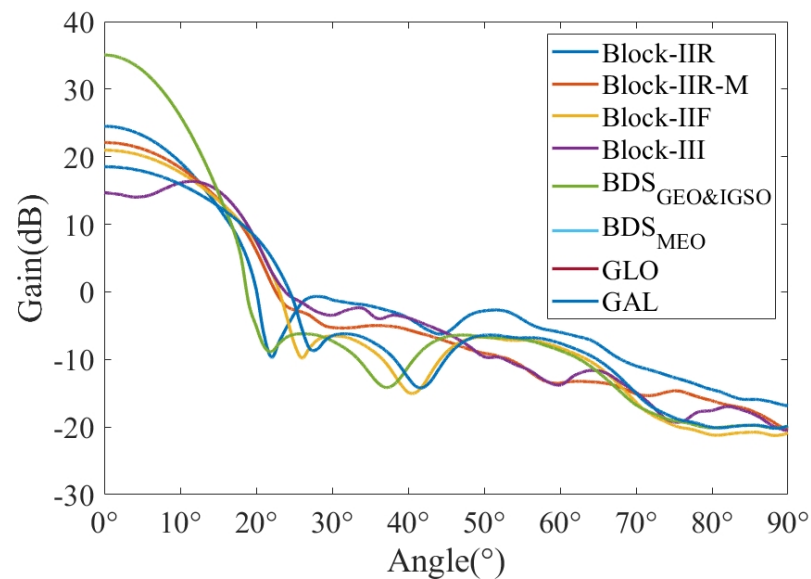


Figure 9. A 2D orientation diagram of different types of antennas after processing.

3.2.4. Receiver Parameter

The receiver parameters are determined by the high-orbit vehicle test communication satellite launched by Beijing Aerospace Flight Control Center, and the specific parameters are shown in Table 4.

Table 4. Receiver parameter table.

Type	Parameter
Antenna polarization pattern	Right-handed circular polarization
Antenna gain	$\pm 40^\circ$ Better than 10 dBi
Axial ratio	<5.2 dB
Standing-wave ratio	≤ 1.5
Joint form	SMA-K
sensitivity	180 dBw
Experience loss	2.2 dBW

3.2.5. Data Processing Center

The final fusion of the data is processed using ground station methods. This approach draws inspiration from the European Space Agency's GENESIS project, which integrates GNSS, SLR, and VLBI technologies on satellites and employs on-board data processing. Our study lays the groundwork for future multi-source fusion detection of deep space environments using low-orbit satellites. In this paper, we adopt ground-based processing methods and utilize the Kalman filter, a recursive filtering algorithm, for data integration.

4. Experiment and Result Analysis

In this paper, experiments are designed and analyzed from the two aspects of visible satellite number and WPDOP, and the visible satellite number simulation experiments of GPS, BDS, GLO, GAL, GPS/BDS/GLO/GAL, SLR station, and VLBI station are designed under the simulation environment time, and the adjustable orbit period of each system is analyzed. Real-time WPDOP simulation experiments of the single GNSS system, single SLR system, single VLBI system, GNSS/SLR dual system, GNSS/VLBI dual system, SLR/VLBI dual system, and GNSS/SLR/VLBI system are designed in the simulation environment, and the orbit determination accuracy of each combined system is analyzed.

The specific experimental design is shown in Table 5.

Table 5. Experimental design enumeration.

Parameter	System Type
Number of visible satellites	GPS
	BDS
	GLO
	GAL
	GPS/BDS/GLO/GAL
	SLR
	VLBI
WPDOP	GNSS
	SLR
	VLBI
	GNSS/SLR
	GNSS/VLBI
	SLR/VLBI
	GNSS/SLR/VLBI

According to the method analysis, the WPDOP value reflects the positioning accuracy, which is positively correlated with the orbit determination accuracy. The accuracy and lifting times of the experimental analysis are represented by the WPDOP value.

4.1. Number of Visible Satellites

The number of visible satellites simulated through the above conditions is shown in Figure 10a, where the number of visible satellites represents the satellites that can be captured and tracked by high-orbit spacecraft (as shown in Table 1). It can be seen that GNSS satellite resources for observation of high-orbit spacecraft are very sparse. At times, there are instances when the number of visible satellites is negligible or even zero, and the average number of visible satellites in a day is 6.9. The epochs satisfying the minimum requirements for single-point positioning account for 73.03% of the total observation period. These requirements are met when there are more than four visible satellites for a single-system configuration, more than five visible satellites for a dual-system configuration, more than six visible satellites for a triple-system configuration, or more than seven visible satellites for a quad-system configuration, so it is very necessary for the multi-source system to provide additional navigation and positioning information to assist orbit determination.

Figure 10b,c respectively represent the number of SLR stations and VLBI ground stations visible to high-orbit spacecraft. The maximum number of SLR stations and VLBI ground stations is six, and the maximum number of VLBI ground stations is four. It can be seen that the number of the two has a roughly similar trend over time. In some sessions (1.1 20:00:00–1.1 21:07:30, 1.2 9:48:00–1.3 8:55:00, 1.5 10:20:30–1.5 23:01:30, 1.6 10:12:30–1.6) 20:00:00), the number of visible observation stations of SLR and VLBI is greater than three, respectively, which meets the condition of single-system positioning.

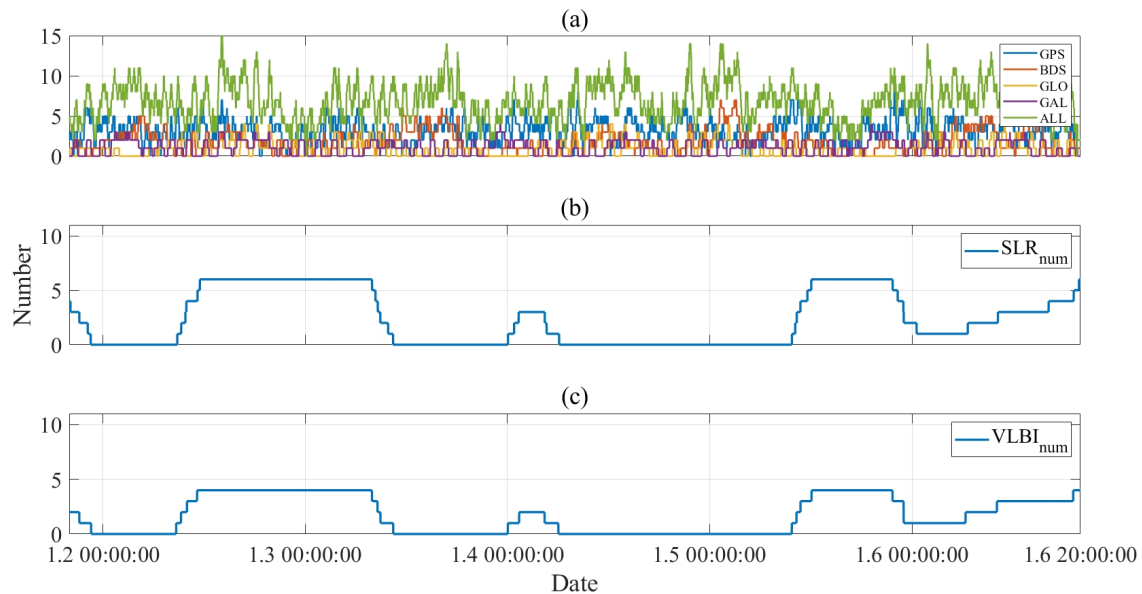


Figure 10. (a) GPS/BDS/GLO/GAL digital maps are available from 0:00 on 1 January 2024 to 23:30 on 1 January 2024. (b) Visible number of SLR stations from 0:00 on 1 January 2024 to 23:30 on 1 January 2024. (c) Visible number of VLBI stations from 0:00 on 1 January 2024 to 23:30 on 1 January 2024.

4.2. Single-System Orbit Determination Analysis

The WPDOP of Single-System

According to the above simulation conditions, the WPDOP values of the GNSS single system, SLR single system and VLBI single system can be simulated during the period from 20:00:00 on 1 January 2024 to 20:00:00 on 6 January 2024, and then the orbit determination performance of each system can be analyzed.

Figure 11a shows the simulation of the WPDOP value of the high-orbit vehicle by GNSS. It can be found that the WPDOP value fluctuates greatly with the change in time, and the orbitability conditions of each period are not met; only 73.03% of the period meets the orbitability conditions, so the observation data can be used to provide positioning data. The longest continuous observation period, defined as the uninterrupted time interval, is 506.5 min, during which the high-orbit vehicle was almost over the Asian region, due to the fact that the GEO and IGSO of BDS satellites were unable to provide observation data. This is because the high-orbit vehicle only uses the leakage signal of the Earth's opposite side satellite for navigation, and the navigation logic is different from that of the Earth. The average value of WPDOP is 1.43×10^2 , the maximum value is 1.76×10^3 , and the minimum value is 35.99. A total of 73.03% of the time is the normal value of detection, and WPDOP is less than three times the mean value. The remaining 1.63% time is the abnormal fixed point of more than three times the standard deviation value, of which the longest abnormal period is 117.5 min, that is, 117.5 min provide positioning data with large errors.

At the same time, the average positioning accuracy obtained through single point positioning is 1.42×10^2 m, indicating that the WPDOP value is nearly equivalent to the positioning accuracy. This further confirms that WPDOP can be used to simply study orbit determination accuracy in this paper.

Figure 11b shows the SLR simulation of the WPDOP value for high-orbit spacecraft. It can be found that the WPDOP value fluctuates gently over time. The average WPDOP value is 7.76×10^2 , the maximum WPDOP value is 6.61×10^6 , and the minimum WPDOP value is 5.22×10^2 , which does not meet the conditions of orbit determination in each period. Only 32.39% of the time period meets the conditions for orbit determination, and the longest time period is 1334.5 min or 22.24 h, which is determined by the SLR ground stations only distributed in China.

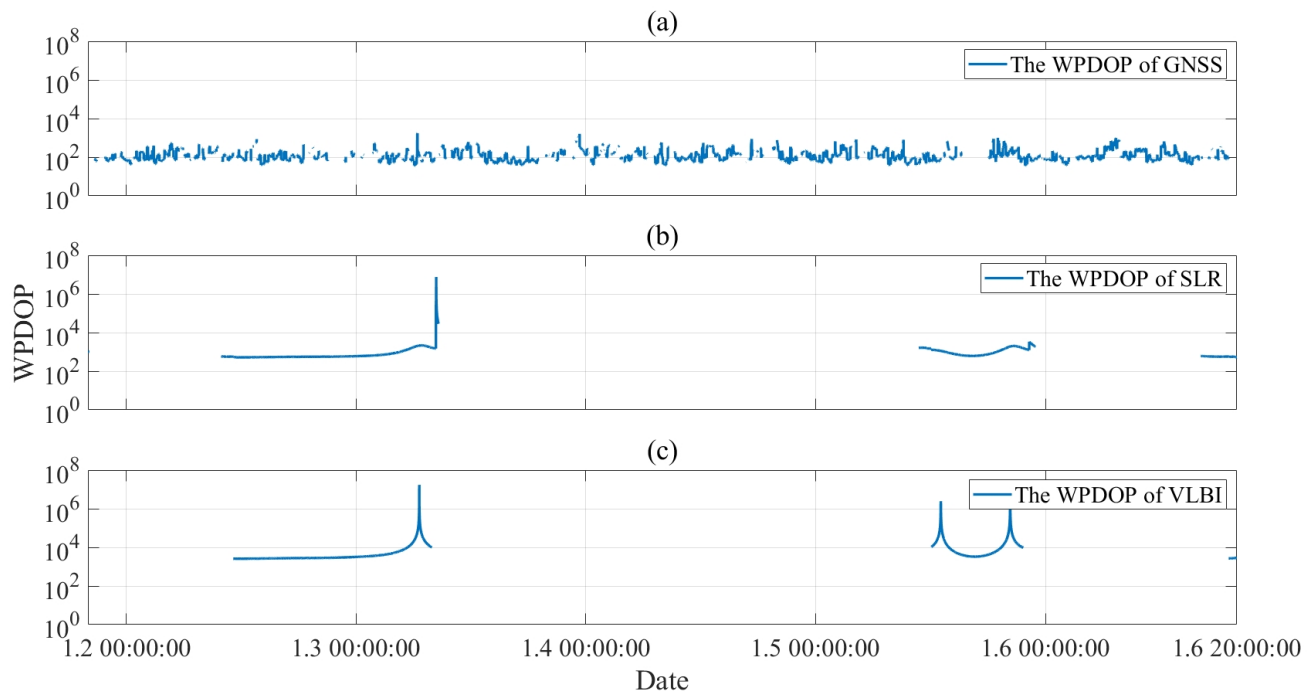


Figure 11. WPDOP values of single GNSS, single SLR and single VLBI systems for high-orbit vehicles. (a) WPDOP value of single GNSS system for high-orbit vehicles. (b) WPDOP value of single SLR system for high-orbit vehicles. (c) WPDOP value of single VLBI system for high-orbit vehicles.

Figure 11c shows the VLBI simulation of the WPDOP value of high-orbit spacecraft. It can be found that the WPDOP value fluctuates relatively smoothly with time change, but the anomalies are extremely obvious. This is because in the detection environment of high-orbit spacecraft, only a small number of ground VLBI measurement stations in China are used, and their geometric configuration is poor. At the same time, the conditions of orbit determination for each period are not met; only 28.85% of the time period meets the conditions of orbit determination, and the longest time period is 3083.3 min, or 51.39 h, and is unable to provide the positioning observation data. The average value of WPDOP is 1.91×10^4 , the maximum value is 3.43×10^7 , and the minimum value is 5.17×10^3 . A total of 26.10% of the time is the normal value of detection, and WPDOP is less than three times the mean value, and the remaining 2.75% time is the abnormal anchor point of more than three times the mean value, among which the longest abnormal period is 24.5 min, that is, the 24.5 min provide positioning data with large errors.

In conclusion, under the premise of single-system orbit determination for high-orbit spacecraft, GNSS has the lowest WPDOP average and the best orbit determination performance, which meets the full-time positioning, followed by SLR, with 32.39% of the detection normal value, and VLBI has the worst orbit determination performance, with only 26.10% of the detection normal value.

4.3. Multi-System Orbit Determination Analysis

4.3.1. The WPDOP of GNSS/VLBI

Figure 12 shows the WPDOP value simulation of the high-orbit vehicle by GNSS/VLBI dual system, and the comparison with GNSS single system and VLBI single system. The blue curve shows the WPDOP value simulation of the high-orbit vehicle by the GNSS/VLBI dual system. The red curve is the WPDOP value simulation of the GNSS single system on the high-orbit vehicle, and the green curve is the WPDOP value simulation of the VLBI single system on the high-orbit vehicle. It can be found that the WPDOP value fluctuates more gently over time than that of the two single systems. The average value of WPDOP is 0.99×10^2 , the maximum value is 1.63×10^3 , and the minimum value is 18.78. Moreover,

there are fewer anomalies, almost none, accounting for only 2.72% of the time, and the longest anomaly period is only 196.0 min, which is smaller than the observation of the GNSS single system or VLBI single system. At the same time, the time period satisfying the conditions of orbit determination is longer, and 86.53% of the time period meets the requirements of orbit determination.

During the whole simulation period, the accuracy of the dual system is improved by about two orders of magnitude compared with the single VLBI system. Compared with the GNSS system with higher accuracy, the accuracy of the dual system is improved from 143 m to 99 m on average, indicating that the positioning accuracy provided by the GNSS/VLBI dual system has improved to a certain extent. The accuracy is improved by about 1.44 times, and the average WPDOP of the single GNSS system is 100.38 during the orbit determination period of the single VLBI system, while the average WPDOP of the dual system is 35.52, and the accuracy is improved by 2.83 times.

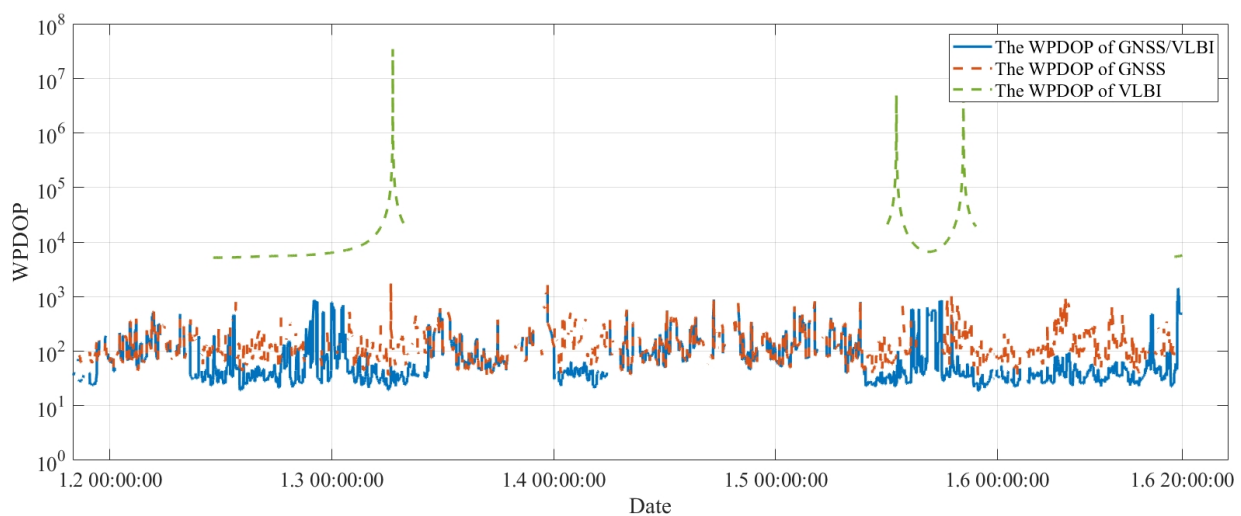


Figure 12. WPDOP value of GNSS and VLBI dual system for high-orbit vehicle.

4.3.2. The WPDOP of GNSS/SLR

Figure 13 shows the WPDOP value simulation of the high-orbit vehicle by the GNSS/SLR dual systems, and the comparison with GNSS single system and SLR single system. The blue curve is the WPDOP value simulation of the high-orbit vehicle by the GNSS single system; the red curve is the WPDOP value simulation of the high-orbit vehicle by the GNSS single system. The green curve is the simulation of WPDOP value of SLR single system for high-orbit vehicle. It can be found that with the change in time, the fluctuation of WPDOP is relatively unchanged. The average value of WPDOP is 1.29×10^2 , the maximum value is 3.64×10^3 , and the minimum value is 1.94. There are also fewer anomalies, almost none, accounting for only 1.91% of the time, and the longest anomaly period is only 137.5 min, which is smaller than the observation of the GNSS single system or SLR single system. At the same time, the time period satisfying the conditions of orbit determination is longer, and 88.97% of the time period meets the requirements of orbit determination.

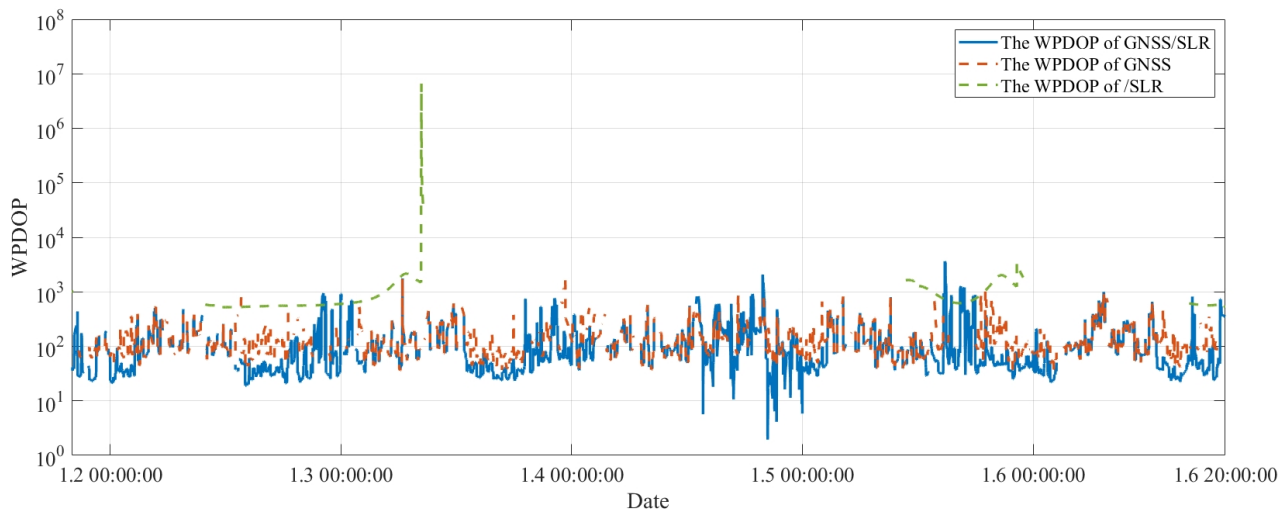


Figure 13. WPDOP value of GNSS and SLR dual system for high-orbit vehicle.

For the dual system combined with GNSS/SLR, the precision of the dual system is slightly higher than that of the GNSS single system. Compared with the single SLR system, the precision of the dual system is improved by an order of magnitude in terms of speed. During the SLR orbit determination period, the average WPDOP of the single GNSS system is 100.38, while that of the dual system is 34.33. The accuracy is improved by 2.92 times. It is similar to the performance of the GNSS/VLBI dual system, indicating that under the precondition of the detection accuracy of each system set by the current simulation, the detection strategy of high-orbit spacecraft can be selected according to the actual conditions of the GNSS/SLR dual system or GNSS/VLBI dual system.

4.3.3. The WPDOP of VLBI/SLR

Figure 14 shows the WPDOP value simulation of the SLR/VLBI dual system for high-orbit spacecraft, and the comparison with the SLR single system and VLBI single system. The blue curve is the WPDOP value simulation of the SLR/VLBI dual system for high-orbit spacecraft, and the red curve is the WPDOP value simulation of the SLR single system for high-orbit spacecraft. The green curve is the WPDOP value simulation of the VLBI single system for a high-orbit vehicle. It can be found that with the change in time, the WPDOP value of the dual system is improved by at least two orders of magnitude in accuracy compared with the SLR of the single system. The average WPDOP is only 26.67 during the time when the two orbits can be determined separately. And compared with the single system, the advantage is that the orbit determination period has increased, accounting for 48.65% of the time, which can meet the orbit determination capability of the high-orbit vehicle in half of the time.

If only the accuracy requirements are considered, the SLR/VLBI dual system is the optimal solution, and the accuracy is 3 to 4 times that of GNSS/SLR and GNSS/VLBI. If the requirements of the observable measurement orbit time are considered, the other two dual system observation strategies can be given priority, which further increases the observable measurement orbit time. The simultaneous use of GNSS has the advantage of one-to-many target detection, which SLR and VLBI do not have.

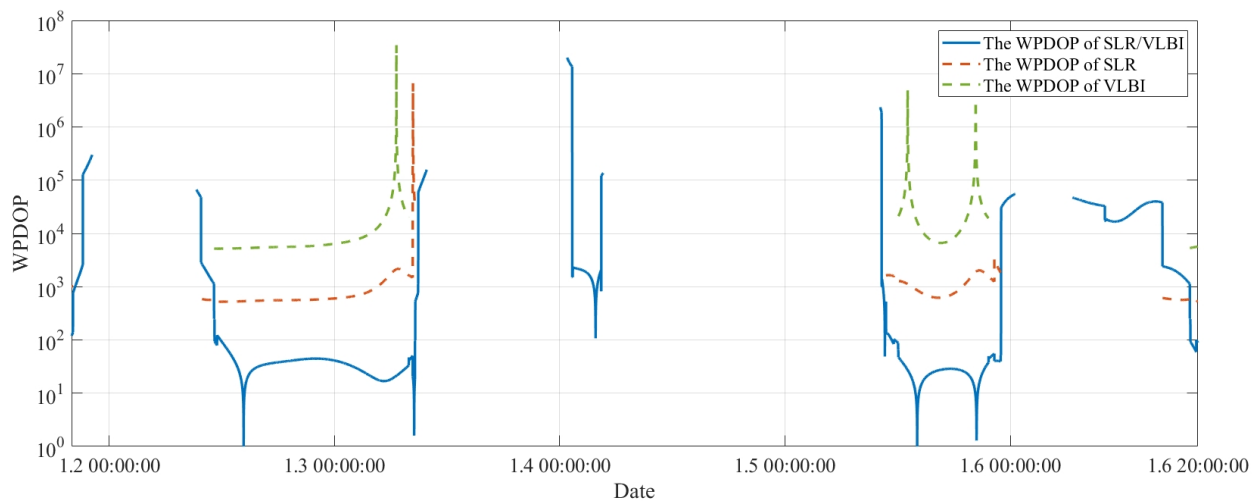


Figure 14. The WPDOP value of the SLR and VLBI dual system for a high-orbit vehicle.

4.3.4. The WPDOP of GNSS/SLR/VLBI

Figure 15 shows the WPDOP value simulation of a high-orbit vehicle by the GNSS/SLR/VLBI system, and the comparison with a GNSS/SLR dual system, GNSS/VLBI dual system, and SLR/VLBI dual system. The blue curve shows the WPDOP value simulation of a high-orbit vehicle by the GNSS/SLR/VLBI system. The curve of the GNSS/SLR dual system is red, the green curve is the WPDOP value simulation of the GNSS/VLBI dual system on the high-orbit vehicle, and the yellow curve is the WPDOP value simulation of the SLR/VLBI dual system on the high-orbit vehicle.

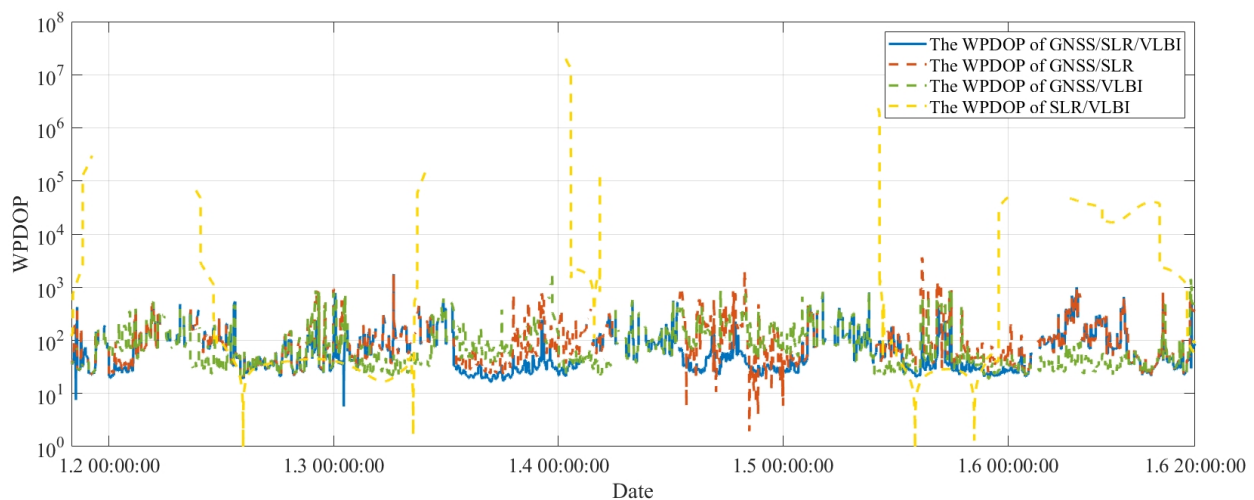


Figure 15. WPDOP values of GNSS, SLR, and VLBI systems for high-orbit spacecraft.

It can be found that with the change in time, the WPDOP value of the three systems is relatively slightly improved. In the period of single SLR or single VLBI orbit determination, the average WPDOP value of the three systems is 34.21, which hardly improves the accuracy compared with the GNSS/SLR and GNSS/VLBI dual systems. However, the accuracy is not as good as that of the SLR/VLBI dual system. In the single SLR or single VLBI undefinable orbit period, the accuracy of the three systems is improved by about two times compared with the GNSS/SLR dual system, the accuracy of the three systems is improved by about three times compared with the GNSS/VLBI dual system, and the accuracy of the SLR/VLBI dual system is improved by about two orders of magnitude compared with the SLR/VLBI dual system. In total, 90.58% of the time period meets the requirement of orbit determination, which exceeds the length of the available orbit determination time period of all dual systems.

Considering the orbit detection strategy, during the period when a single SLR can locate the orbit, only the GNSS/VLBI dual system can be used for orbit determination, which has the highest accuracy and the fewest resources. In the remaining period, the three GNSS/SLR/VLBI systems can be considered for orbit determination, which not only meets the requirements of higher accuracy but also meets the requirements of a longer period of orbit observation data.

Given that SLR offers high precision, the integration of three systems may paradoxically result in lower accuracy compared to the dual-system combination of SLR and VLBI. This study specifically examines the impact of the SLR measurement precision on orbit determination accuracy. Initially, a moderate value between 0.01 m and 0.10 m is chosen for SLR measurement precision. However, recognizing that the initially selected 0.05 m (5 cm) precision for SLR measurements may not be optimal, this paper conducts simulation analyses using various SLR measurement precision parameters to better understand their effects.

In Figure 16, δ WPDOP represents the difference between the average WPDOP values of the three-system configuration and the SLR/VLBI dual-system configuration during periods when the orbit determination is possible using SLR alone. As shown in Figure 16a, within the orbit determination arc of the single VLBI system, the difference between the average WPDOP values of the three-system configuration and the single SLR system does not change significantly as the SLR observation precision improves. Figure 16b demonstrates that the SLR measurement precision has minimal impact on the WPDOP difference between the three-system and SLR/VLBI dual-system configurations, indicating that it does not significantly influence the selection of orbit determination observation strategies.

Furthermore, simulations conducted with the SLR measurement precision ranging from 0.01 m to 0.10 m reveal that the average WPDOP value of the three-system configuration during SLR-viable orbit determination periods exhibits only a minute variation of 4.56×10^{-5} . This suggests that when the SLR measurement precision is the sole variable, the WPDOP value of the three-system configuration approaches its corresponding Cramér–Rao lower bound. Consequently, improvements in the SLR measurement precision have minimal effect on the WPDOP values of the three-system configuration.

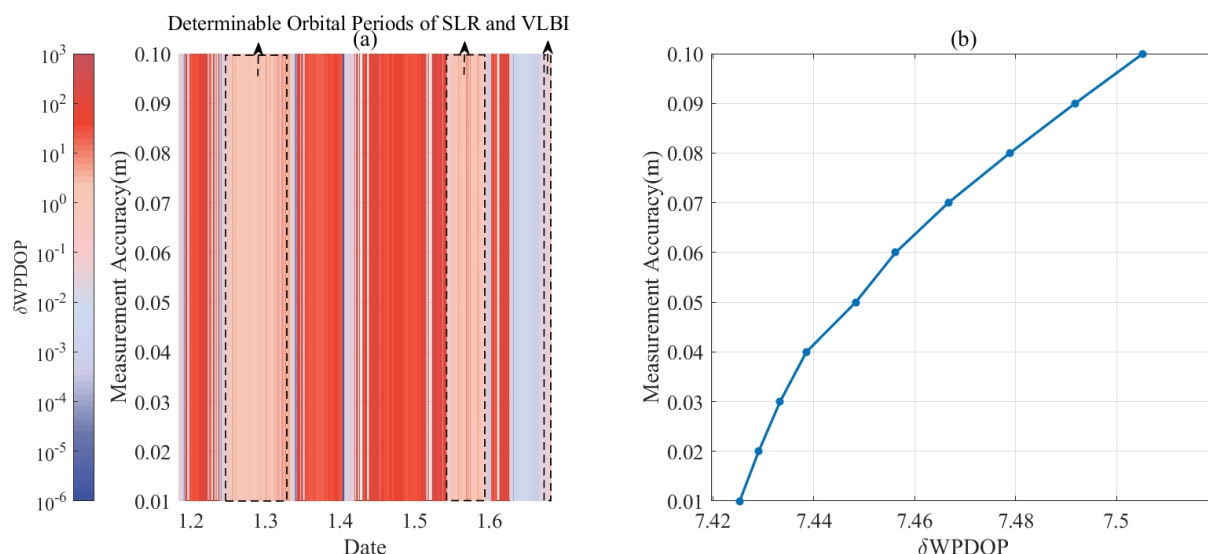


Figure 16. The δ WPDOP values of the three systems and the single SLR vary with the measurement accuracy of the single SLR.

4.4. Summary of Various WPDOP Fusion Strategies

From a scientific research perspective, to further consider the impact of SLR on the orbit determination performance of the three systems, this study selects global SLR stations for comparative analysis. We compile three types of data based on different integration

strategies using Chinese SLR stations and global SLR stations: determinable orbit periods, mean WPDOP values during a trackable period of a single VLBI station, and mean WPDOP values during the non-trackable period of a single VLBI station. The data summary is presented in Figure 17.

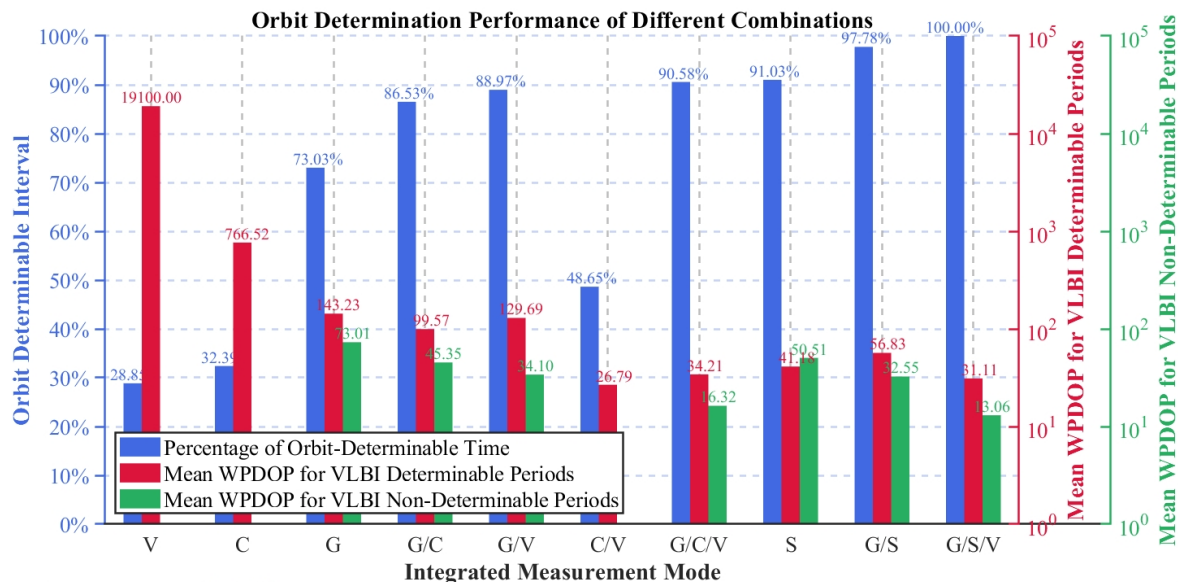


Figure 17. Orbit determination performance of different combinations: V (VLBI), C (Chinese SLR), G (GNSS), S (Global SLR).

When utilizing global SLR stations, the orbit determination performance of all three systems is improved. The determinable orbit periods account for 100% of the total periods, meeting the conditions for full-day orbit determination. During the VLBI determinable periods, the mean WPDOP value is 31.11. However, this still falls short of the precision achieved by the SLR/VLBI dual system. During VLBI indeterminable periods, the mean WPDOP value is 13.06.

4.5. Discussion

Among the three individual systems, GNSS demonstrates the highest single-system orbital determination accuracy with an average WPDOP of 1.43×10^2 , while VLBI shows the lowest accuracy with an average WPDOP of 1.91×10^4 . GNSS offers the longest viable orbital determination period, covering 73.03% of the total duration. The trackable duration for SLR and VLBI is similar, approximately 30% of the total time.

Regarding the three dual-system integration strategies, no single approach exhibits absolute superiority in terms of orbital determination accuracy. Comparatively, the SLR/VLBI dual-system strategy achieves relatively higher accuracy but has the shortest trackable period, covering only 48.65% of the total duration. This strategy may be considered viable under specific conditions.

For the GNSS/SLR/VLBI triple-system orbital determination, the accuracy during the trackable period of a single VLBI station is slightly lower than that of the SLR/VLBI dual system. However, it offers the highest trackable period of 90.58% among all integration forms and demonstrates superior accuracy during the non-trackable period of a single VLBI station, surpassing the GNSS/VLBI dual-system accuracy by twofold. Variations in the SLR ranging accuracy within the 0.01 m–0.10 m range have minimal impact on both the triple-system and SLR/VLBI dual-system accuracies. Transitioning from Chinese SLR stations to global SLR stations positively influences both the trackable period and accuracy, albeit less significantly than anticipated.

5. Conclusions

This paper focuses on the research of precision orbit determination technology of high-orbit spacecraft to meet the research needs of key navigation technologies for space exploration. Decoupled Kalman filtering results indicate a positive correlation between measurement positioning accuracy and orbit determination precision. The derived WPDOP values can, to some extent, equivalently characterize the orbit determination accuracy.

Analysis of the WPDOP values for GNSS, SLR, and VLBI systems reveals that GNSS demonstrates the highest orbit determination accuracy among single systems, with meter-level positioning and the longest visible arc, while VLBI exhibits the lowest, and SLR falls in between. In dual-system fusion strategies, SLR/VLBI orbit determination accuracy holds an absolute advantage, with a mean WPDOP of 26.79. However, the SLR/VLBI dual-system strategy has a relatively low orbit determination duration, covering only 48.65% of the total period, and is thus considered only in specific situations.

The GNSS/SLR/VLBI tri-system orbit determination offers the longest duration and high accuracy, with a mean WPDOP of 34.21, second only to the SLR/VLBI dual-system strategy. Improving the SLR measurement accuracy has a negligible impact on the tri-system orbit determination performance, with a δ WPDOP of only 4.56×10^{-5} when the SLR measurement accuracy varies from 0.01 to 0.10 m. Furthermore, utilizing global SLR station data positively affects tri-system performance, albeit marginally, reducing the mean WPDOP to 31.11. However, this option is not considered due to the significant increases in cost and resource consumption.

Consequently, when within the trackable period of a single VLBI station, the SLR/VLBI dual-system orbit determination strategy is preferred. During the non-trackable period of a single VLBI station, the GNSS/SLR/VLBI tri-system strategy is recommended. Merely increasing the SLR measurement accuracy and global station distribution has limited impact on GNSS/SLR/VLBI tri-system high-orbit vehicle orbit determination; the same applies to VLBI.

To further enhance tri-system orbit determination performance, optimizing SLR and VLBI station geometric distribution is necessary. This provides essential support for developing SLR and VLBI technologies for low-orbit satellites. These findings offer valuable reference for selecting high-orbit vehicle orbit determination schemes and provide crucial guidance for future deep space exploration and navigation system design.

Author Contributions: Z.W. conceived the idea and designed the experiments with S.N., W.X., Z.L. and H.L. W.Z. wrote the main manuscript. W.X. and Z.L. reviewed the paper. All components of this research were carried out under the supervision of S.N. All authors have read and agreed to the published version of the manuscript.

Funding: This research was funded by National Natural Science Foundation of China under Grant grant number U20A0193 and Orbit optimization design and high performance receiving technology of Earth–Moon space navigation system under grant number WXDHS2023108.

Data Availability Statement: The data related to this article are available upon request to the corresponding authors.

Conflicts of Interest: The authors declare no conflicts of interest.

Abbreviations

The following abbreviations are used in this manuscript:

GNSS	Global Navigation Satellite System
VLBI	Very Long Baseline Interferometry
SLR	Satellite laser ranging
TOA	Time of Arrival
LiAISON	Linked Autonomous Interplanetary Satellite Orbit Navigation
INS	Inertial Navigation System
WPDOP	Weighted Position Dilution of Precision

BDS	Beidou Navigation Satellite System
LEO	Low Earth Orbit Satellite
MEO	Middle Earth Orbit Satellite
HEO	High Earth Orbit Satellite
GEO	Geostationary Orbit Satellite
IGSO	Inclined Geosynchronous Orbit Satellite

References

- Wu, W.R.; Liu, W.W.; Qiao, D.; Jie, D. Investigation on the development of deep space exploration. *Sci. China Echnologic. Sci.* **2012**, *55*, 1086–1091. [\[CrossRef\]](#)
- Fu, Y.; Liu, S. Statistics and Analysis of global spacecraft launches in 2019. *Int. Space* **2020**, *2*, 11–15.
- Wang, L.-W.; Guo, D.-W.; Zhang, Z.; Lv, Z.H.; Zhao, M.; Liu, Y. Introduction to NASA's Artemis lunar exploration program. *Spacecr. Recovery Remote Sens.* **2020**, *41*, 1–12.
- Wang, J.; Zhang, Y.; Di, K.L.; Chen, M.; Duan, J.; Kong, J.; Xie, J.; Liu, Z.; Wan, W.; Rong, Z.; et al. Localization of the Chang'e-5 lander using radio-tracking and image-based methods. *Remote Sens.* **2021**, *13*, 590. [\[CrossRef\]](#)
- Laurini, K.C.; Gerstenmaier, W.H. The Global Exploration Roadmap and its significance for NASA. *Space Policy* **2014**, *30*, 149–155. [\[CrossRef\]](#)
- Hauptlik-Meusburgera, S.; Messinab, P. Envisioning the Moon Village-A Space Architectural Approach. In Proceedings of the 69th International Astronautical Congress (IAC), Bremen, Germany, 1–5 October 2018.
- Shi, T.; Zhuang, X.; Xie, L. Performance evaluation of multi-GNSSs navigation in super synchronous transfer orbit and geostationary earth orbit. *Satell. Navig.* **2021**, *2*, 5. [\[CrossRef\]](#)
- Lou, Y.; Dai, X.; Gong, X.; Li, C.; Qing, Y.; Liu, Y.; Peng, Y.; Gu, S. A review of real-time multi-GNSS precise orbit determination based on the filter method. *Satell. Navig.* **2022**, *3*, 15. [\[CrossRef\]](#)
- Li, X.; Dong, Q.; Yu, C. Research progress of three-body orbital dynamics. *Chin. J. Mech. Mech.* **2021**, *53*, 1223–1245.
- Meng, W.; Liu, L.; Tang, D.; Yang, X. Feasibility Analysis and Design of GNSS autonomous navigation for lunar spacecraft. In *Proceedings of the 8th China Satellite Navigation Academic Conference—S04 Satellite Orbit and Clock Difference*, Shanghai, China, 23–25 May 2017; Academic Exchange Center of China Satellite Navigation System Management Office, Beijing Institute of Satellite Information Engineering: Beijing, China, 2017; Volume 5.
- Palmerini, G.B.; Sabatini, M.; Perrotta, G. En route to the Moon using GNSS signals. *Acta Astronaut.* **2009**, *64*, 467–483. [\[CrossRef\]](#)
- Palmerini, G.B. GNSS software receiver as navigation sensor in very high orbits. In Proceedings of the 2014 IEEE Metrology for Aerospace (MetroAeroSpace), Benevento, Italy, 29–30 May 2014.
- Balbach, O.; Eissfeller, B.; Institute of Electric and Electronic Engineer. Tracking GPS above GPS satellite altitude: First results of the GPS experiment on the HEO mission Equator-S. In Proceedings of the IEEE 1998 Position Location and Navigation Symposium (Cat. No.98CH36153), Palm Springs, CA, USA, 20–23 April 1996; IEEE: Piscataway, NJ, USA, 1998.
- Davis, G.; Moreau, M.; Carpenter, R.; Bauer, F. GPS-Based Navigation and Orbit Determination for AMSAT AO-40 Satellite. In Proceedings of the AIAA Guidance, Navigation, and Control Conference and Exhibit, Monterey, CA, USA, 5–8 August 2002.
- Qiang, Q.; Lin, B.; Liu, Y.; Lin, X. Review on autonomous navigation technology for deep space exploration. *Navig. Control.* **2023**, *22*, 19–32.
- Jiang, K. *Research on Precise Orbit Determination of High-Orbit Spacecraft Based on Spaceborne GNSS Weak Signal*; Wuhan University: Wuhan, China, 2020. [\[CrossRef\]](#)
- Wu, W. *Research on Key Technologies of Precise Orbit Determination for Earth-Moon Space Spacecraft Based on Spaceborne GNSS*; China Mining University: Xuzhou, China, 2023.
- Qin, H.; Liang, M. Research on high orbit satellite positioning technology based on GNSS. *Chin. J. Space Sci.* **2008**, *316*–325. [\[CrossRef\]](#)
- Chai, J.; Wang, X.; Yu, N.; Wang, D.; Li, Q. High orbital spacecraft GNSS signal transmission link modeling and strength analysis. *J. Beijing Univ. Aeronaut. Astronaut.* **2018**, *44*, 1496–1503. [\[CrossRef\]](#)
- Sun, Z.; Wang, X. High rail environment GNSS visibility and geometric dilution of precision analysis. *Aviat. Weapon* **2017**, *18*–27. [\[CrossRef\]](#)
- Li, Z.H.; Wei, E.H.; Wang, Z.T. *Spatial Geodesy*; Wuhan University Press: Wuhan, China, 2010; pp. 100–101.
- Ma, P.; Baoyin, H.; Mu, J. Autonomous navigation of Mars probe based on optical observation of Martian moon. *Opt. Precis. Eng.* **2014**, *22*, 863–869.
- Mastrodemos, N.; Kubitschek, D.G.; Synnott, S.P. Autonomous navigation for the deep impact mission encounter with comet Tempel-1. *Space Sci. Rev.* **2005**, *117*, 95–121. [\[CrossRef\]](#)
- Yu, P.; Zhang, H.H.; Li, J.; Guan, Y.F.; Wang, L.; Zhao, Y.; Chen, Y.; Yang, W.; Yu, J.; Wang, H.Q. Design and implementation of GNC system of lander and ascender module of Chang'e-5 spacecraft. *Sci. Sin. Technol.* **2021**, *51*, 763–777. [\[CrossRef\]](#)
- Zhao, Y.; Wang, X.; Huang, X. Tianwen-1 lander guidance navigation and control system for Mars soft landing. *Aerosp. Control. Appl.* **2021**, *47*, 48–57.
- Wang, M.; Zheng, X.; Cheng, Y.; Chen, X. Scheme and key technologies of autonomous optical navigation for Mars exploration in cruise and capture phase. *Geomat. Inf. Sci. Wuhan Univ.* **2016**, *41*, 434–442.

27. Battin, R.H. *An Introduction to the Mathematics and Methods of Astrodynamics*; American Institute of Aeronautics and Astronautics: Washington, DC, USA, 1999.
28. Zhang, W.; Chen, X.; You, W.; Fang, B. New autonomous navigation method based on redshift. *Aerosp. Shanghai* **2013**, *30*, 32–33+38.
29. Zhang, W. A study of the navigation technology and application based on astronomical spectral velocity measurement. *Navig. Control.* **2020**, *19*, 64–73.
30. Li, T.P.; Xiong, S.L.; Zhang, S.N.; Lu, F.; Song, L.; Cao, X.; Chang, Z.; Chen, G.; Chen, L.; Chen, T.; et al. Insight-HXMT observation of the first binary neutron star merger GW170817. *Sci. China Phys. Mech. Astron.* **2018**, *61*, 031011. [[CrossRef](#)]
31. Hill, K.A. *Autonomous Navigation in Libration Point Orbits*; University of Colorado at Boulder: Boulder, CO, USA, 2007.
32. Bahder, T.B. Quantum Positioning Systems and Methods. U.S. Patent 7,359,064, 15 April 2008.
33. Capuano, V.; Botteron, C.; Wang, Y.; Tian, J.; Leclerc, J.; Farine, P.-A. GNSS/INS/Star tracker integrated navigation system for earth-moon transfer orbit. In Proceedings of the 27th International Technical Meeting of the Satellite Division of The Institute of Navigation (ION GNSS+ 2014), Tampa, FL, USA, 8–12 September 2014; pp.1433–1447.
34. Capuano, V.; Shehaj, E.; Botteron, C.; Blunt, P.; Farine, P.-A. GNSS/INS/Star tracker integration for real-time on-board autonomous orbit and attitude determination in LEO, MEO, GEO and beyond. In Proceedings of the 68th International Astronautical Congress, Adelaide, Australia, 25–29 September 2017.
35. Capuano, V.; Opromolla, R.; Cuciniello, G.; Pesce, V.; Sarno, S.; Capuano, G.; Lavagna, M.; Grassi, M.; Corrado, F.; Tabacco, P.; et al. A highly integrated navigation unit for on-orbit servicing missions. In Proceedings of the International Astronautical Congress, Bremen, Germany, 1–5 October 2018.
36. Giordano, P.; Malman, F.; Swinden, R.; Zoccarato, P.; Ventura-Traveset, J. The Lunar Pathfinder PNT experiment and on light navigation service: The future of Lunar position, navigation and timing. In Proceedings of the 2022 International Technical Meeting of the Institute of Navigation, Long Beach, CA, USA, 25–27 January 2022.
37. Parker, J.J.; DAVIS, F.; Anderson, B.; Ansalone, L.; Ashman, B.; Bauer, F.H.; D’amore, G.; Facchinetti, C.; Fantinato, S.; Impresario, G.; et al. The Lunar GNSS Receiver Experiment (LuGRE). In Proceedings of the Institute of Navigation International Technical Meeting, Long Beach, CA, USA, 25–27 January 2022.
38. Zhao, F. *Research on Nonlinear Filtering Algorithm for Autonomous Navigation*; University of Electronic Science and Technology of China: Chengdu, China, 2020.
39. Geng, Y.; Zhang, D. Review of adaptive filtering algorithms. *Inf. Electron. Eng.* **2008**, *64*, 315–320.
40. Long, A.C.; Cappellari, J.O.; Velez, C.E.; Fuchs, A.J. Goddard Trajectory Determination System (GTDS) Mathematical Theory (Revision 1). Available online: http://www.amsat-bda.org/files/gtds_math_theory_jul89.pdf (accessed on 8 September 2024).
41. Tuckness, D.G.; Young, S.Y. Autonomous navigation for lunar transfer. *J. Spacecr. Rocket.* **1995**, *32*, 279–285. [[CrossRef](#)]
42. Shi, J.; Li, Y.Y.; Qi, G.Q.; Sheng, A. Extended target tracking filter with intermittent observations. *IET Signal Process.* **2016**, *10*, 592–602. [[CrossRef](#)]
43. Zhao, F.F.; Ge SZ, S.; Zhang, J.; He, W. Celestial navigation in deep space exploration using spherical simplex unscented particle filter. *IET Signal Process.* **2018**, *12*, 463–470. [[CrossRef](#)]
44. Gao, Y.; Krakiwsky, E.J.; Abousalem, M.A.; McLellan, J.F. Comparison and analysis of centralized, decentralized, and federated filters. *Navigation* **1993**, *40*, 69–86. [[CrossRef](#)]
45. Gao, B.; Hu, G.; Gao, S.; Zhong, Y.; Gu, C. Multi-sensor optimal data fusion for INS/GNSS/CNS integration based on unscented Kalman filter. *Int. J. Control. Autom. Syst.* **2018**, *16*, 129–140. [[CrossRef](#)]
46. Hu, G.; Xu, L.; Gao, B.; Chang, L.; Zhong, Y. Robust unscented Kalman filter-based decentralized multisensor information fusion for INS/GNSS/CNS integration in hypersonic vehicle navigation. *IEEE Trans. Instrum. Meas.* **2023**, *72*, 8504011. [[CrossRef](#)]
47. Ning, X.; Wang, L.; Wu, W.; Fang, J. A celestial assisted INS initialization method for lunar explorers. *Sensors* **2011**, *11*, 6991–7003. [[CrossRef](#)]
48. Donaldson, J.E.; Parker, J.K.; Moreau, M.C.; Highsmith, D.E.; Martzen, P. Characterization of On-Orbit GPS Transmit Antenna Patterns for Space Users. In Proceedings of the ION GNSS, Miami, FL, USA, 24–28 September 2018.

Disclaimer/Publisher’s Note: The statements, opinions and data contained in all publications are solely those of the individual author(s) and contributor(s) and not of MDPI and/or the editor(s). MDPI and/or the editor(s) disclaim responsibility for any injury to people or property resulting from any ideas, methods, instructions or products referred to in the content.

Copyright of Remote Sensing is the property of MDPI and its content may not be copied or emailed to multiple sites or posted to a listserv without the copyright holder's express written permission. However, users may print, download, or email articles for individual use.